# The X-ray Afterglows of GRB 020813 and GRB 021004 with Chandra HETGS: Evidence for a Supernova Prior to GRB 020813

Nathaniel R. Butler<sup>1</sup>, Herman L. Marshall<sup>1</sup>, George R. Ricker<sup>1</sup>, Roland K. Vanderspek<sup>1</sup>, Peter G. Ford<sup>1</sup>, Geoffrey B. Crew<sup>1</sup>, Donald Q. Lamb<sup>2</sup>, J. Garrett Jernigan<sup>3</sup>

nrbutler@space.mit.edu, hermanm@space.mit.edu, grr@space.mit.edu,
roland@space.mit.edu, pgf@space.mit.edu, gbc@space.mit.edu,
lamb@pion.uchicago.edu, jgj@ssl.berkeley.edu

## ABSTRACT

We detect emission lines from hydrogen-like sulfur (S XVI) and hydrogen-like silicon (Si XIV) in a 76.8 ksec Chandra HETGS spectrum of the afterglow of GRB 020813. The probability that these features are due to random Poisson fluctuations is estimated to be <0.01%. Ni is observed at low significance, but Fe is not detected. A thermal model fits the data adequately, but a reflection model may provide a better fit. There is marginal evidence that the equivalent widths of the emission lines decrease as the burst fades. We infer from these results that a supernova likely occurred  $\sim 2$  months prior to the GRB. We find no discrete or variable spectral features in the Chandra HETGS spectrum of the GRB 021004 afterglow.

Subject headings: gamma rays: bursts — supernovae: general — X-rays: general

## 1. Introduction

Much evidence has accumulated in recent years connecting long-duration  $\gamma$ -ray bursts (GRBs) (Kouveliotou et al. 1993) to progenitor supernovae (SNe). The detection of SN

<sup>&</sup>lt;sup>1</sup>Center for Space Research, Massachusetts Institute of Technology, Cambridge, MA 02139

<sup>&</sup>lt;sup>2</sup>Department of Astronomy & Astrophysics, University of Chicago, Chicago, IL 60637

<sup>&</sup>lt;sup>3</sup>Space Sciences Laboratory, University of California, Berkeley, CA 94720

1998bw in association with GRB 980425 (Galama et al. 1998) and the detection of late-time SN "bumps" in several afterglow light curves (Bloom et al. (1999), Reichart (2001) and references therein), the observed positional coincidences between star-forming regions and long-duration GRB afterglows (e.g. Sahu et al. (1997), Kulkarni et al. (1998), Kulkarni et al. (1999)), the evidence for dust extinction in some GRB afterglows, and the recent discovery of multiple- $\alpha$  elements (Mg, Si, S, Ar, Ca) in the *XMM-Newton* (Jansen et al. 2001) spectrum of GRB 011211 (Reeves et al. 2002) (with additional possible detections by Watson et al. (2002)), all point toward GRBs exploding in or near supernova remnants (SNRs). Several authors (e.g. Vietri et al. (2001), McLaughlin et al. (2002)) suggest the reinterpretation of the Fe-K lines reported in the X-ray afterglows of recent GRBs (Piro et al. (1999), Piro et al. (2000), Antonelli et al. (2002)) as K-lines from Ni or Co. This interpretation may be consistent with the supra-nova (Vietri & Stella 1999) model for GRB origins, in which the GRB follows a recent and failed SN explosion, possibly prior to significant formation of Fe<sup>56</sup>.

Beyond very weak evidence in Piro et al. (2000) for an emission line from H-like S in GRB 991216, Reeves et al. (2002) (hereafter R02) are the first to strongly assert evidence for emission from low-Z elements in a GRB X-ray afterglow. If valid, this claim has broad implications for GRB emission models and it would strongly link GRBs to SNe. The reduction of these data and the statistical significance of the results has been called into question by Borozdin & Trudoyubov (2002) and Rutledge & Sako (2002), respectively. In a follow-up paper (Reeves et al. 2002b), the *XMM-Newton* observers address those concerns. Physical interpretations aside, the R02 results are controversial largely due to the small number of observed counts and the low spectral resolution of the EPIC-pn instrument, which would blur some fraction of the line emission into the continuum. These hinder an accurate measurement of the continuum emission and make it difficult to gauge the significance of discrete spectral features.

We find evidence for Si and S (and possibly Ar and Ca) emission in the Chandra X-ray Observatory (Weisskopf et al. 2002) High Energy Transmission Grating Spectrometer (HETGS) spectrum of the GRB 020813 afterglow. We detect a Ni-K line at low significance and find a strikingly low upper limit to the Fe-K line equivalent width. The emitting material is blue-shifted with velocity  $\sim 0.1c$  relative to the GRB host galaxy. These results add weight to the detections claimed by R02 and Watson et al. (2002). With the HETGS's high spectral resolution, we are able to resolve the line widths, and we are able to accurately separate the line and continuum emission. Because the lines we associate with S and Si are detected in the full data set, we have  $\sim 5 \times$  more counts to work with than R02, where the line emission is observed during only a short period of time. Moreover, the continuum is an order of magnitude stronger than that reported by R02, possibly indicating, in the case of thermal emission, that a power-law component is also present. This may alternatively be a sign that

the lines are produced under reflection.

## 2. Observations

Using Directors Discretionary Time, two afterglows of GRBs detected by the *High-Energy Transient Explorer* (*HETE* ) (Ricker et al. 2003) were observed with the *Chandra* HETGS, approximately 1 day after each burst, and lasting for approximately 1 day. Both bursts were long-duration GRBs, with  $\gamma$ -ray durations  $\gtrsim 100s$ . The  $\gamma$ -ray peak flux from GRB 020813 (Villasenor et al. 2002) was quite high ( $\sim 10^{-5}$  ergs cm<sup>-2</sup> s<sup>-1</sup>), while the peak flux from GRB 021004 (Shirasaki et al. 2002) was approximately two orders of magnitude lower.

Chandra began observing the GRB 020813 afterglow with the HETGS on August 13.990 ( $t_{burst}+21.02~{\rm hrs}$ ) and continued until August 14.892 ( $t_{burst}+42.67~{\rm hrs}$ ), with a total livetime of 76.8 ksec. The mean count rate from the HEG and MEG gratings and the 0th-order image was 0.12 counts/s. The afterglow candidate reported by Fox (2002a) was detected and was observed to fade in brightness with time according to a power-law of index  $\alpha=-1.38\pm0.06~(\chi^2_{\nu}=36.4/24)$ , consistent with the value reported by Vanderspek et al. (2002) and consistent with measured values in the optical (Malesani et al. 2002). Between 0.6 and 6 keV, we measure a time-averaged flux of  $1.9\times10^{-12}~{\rm ergs~cm^{-2}~s^{-1}}$ .

As first reported by Sako & Harrison (2002), Chandra began observing the afterglow of GRB 021004 on October 5.358 ( $t_{burst}$  + 20.49 hrs) and continued until October 6.400 ( $t_{burst}$  + 45.50 hrs), with a total livetime of 86.7 ksec. The mean count rate from the HEG and MEG gratings and the 0th-order image was 0.036 counts/s. The afterglow candidate reported by Fox (2002b) was detected and was observed to fade in brightness with time. The X-ray light curve appears variable. (Similar variability has been reported in the optical for this afterglow; see e.g. Halpern et al. (2002)). The temporal fade in flux can be described by a power-law with index  $\alpha = -0.9 \pm 0.1$  ( $\chi^2_{\nu} = 83.8/27$ ), consistent with the values reported by Sako & Harrison (2002) and Holland et al. (2002). The time-averaged flux between 0.6 and 6 keV is measured to be  $5.7 \times 10^{-13}$  ergs cm<sup>-2</sup> s<sup>-1</sup>.

The total number of counts detected by *Chandra* in the case of GRB 020813 (GRB 021004) is  $\sim 9 \times (3 \times)$  the number of counts detected for GRB 991216 (Piro et al. 2000). We perform a parallel spectral/temporal analysis below for the X-ray afterglow spectra of GRB 020813 and GRB 021004.

## 3. Spectral Fitting

We reduce the HETGS spectral data from the standard L2 event lists using IDL and custom scripts, described in Marshall et al. (2002). For the 0th-order spectral data, we use the CIAO<sup>4</sup> processing exclusively. Each data set is corrected for QE degradation<sup>5</sup> due to contamination in the ACIS chips, prior to spectral fitting. We also destreak the S4 chip<sup>6</sup>. Spectral fitting and analysis is performed with ISIS<sup>7</sup>. For each observation, we fit the HETGS HEG and HETGS MEG 1st-order data for the entire observation jointly. The +1 and -1orders are combined for each grating. The data are then binned to a  $S/N \geq 5$  per bin, with the bin width restricted to  $\delta E/E \leq 0.1$ . We define S/N as the background-subtracted number of counts divided by the square root of the sum of the signal counts and the variance in the background. Bins of the maximal width with S/N < 3 are rejected, due to lack of signal. For GRB 021004, we retain bins down to S/N= 2.5. For GRB 020813, this selects an HEG energy range of 0.8-7.6 keV and and MEG energy range of 0.6-5.2 keV. For GRB 021004, this selects an HEG energy range of 1.0-4.6 keV and and MEG energy range of 0.6-4.7 keV. We remove the instrumental response corresponding to each observation prior to fitting by dividing the binned counts data by the averaged ARF (ancillary response file). We then fit each model by minimizing  $\chi^2$ . Unless otherwise noted, all quoted errors are 90% confidence.

### 3.1. GRB 020813

As reported by Vanderspek et al. (2002), we find that an absorbed power-law fit to the 1st-order spectra requires no absorption column in excess of Galactic value. Therefore, in each model that we consider, we include absorption with  $N_{\rm H}$  frozen to  $7.5 \times 10^{20}$  cm<sup>-2</sup>.

The data are moderately well fit by a power-law (Figure 1,  $\chi^2_{\nu} = 176.0/154$ ), with photon index  $\Gamma = 1.85 \pm 0.04$  and normalization  $(5.5 \pm 0.2) \times 10^{-4}$  photons/keV/cm<sup>2</sup>/s at 1 keV. A thermal bremsstrahlung fit is a much poorer fit to the data ( $\chi^2_{\nu} = 196.7/154$ , rejectable at 99% confidence), with  $kT = 4.6 \pm 0.5$  keV. We find consistent fits using the 0th order data. Of note, a large fraction of the contribution to  $\chi^2$  in the case of the HETGS power-law fit arises between 1.2 and 1.5 keV. The addition of a Gaussian component in

<sup>&</sup>lt;sup>4</sup>http://cxc.harvard.edu/ciao/

<sup>&</sup>lt;sup>5</sup>http://asc.harvard.edu/cal/Acis/Cal\_prods/qeDeg/

<sup>&</sup>lt;sup>6</sup>http://asc.harvard.edu/ciao/threads/spectra\_hetgacis/

<sup>&</sup>lt;sup>7</sup>http://space.mit.edu/CXC/ISIS/

this energy range improves the  $\chi^2$  ( $\chi^2_{\nu}=160.5/151$ ). The line energy is  $1.31\pm0.01$  keV, with a width of  $8\pm4$  eV ( $1\sigma$ ). The rest-frame equivalent width is  $67\pm32$  eV, and the flux is  $(1.6\pm0.8)\times10^{-14}$  ergs cm<sup>-2</sup> s<sup>-1</sup>. Given the optically measured GRB host galaxy absorption redshift  $z\geq1.254$  (Price et al. 2002), a likely association for this line is S XVI K $\alpha$ , blue-shifted by 0.12c from z=1.254. The  $\chi^2$  is further improved ( $\chi^2_{\nu}=155.7/150$ ) with the inclusion of an additional Gaussian component of the same width, constrained to lie at predicted energy of Si XIV K $\alpha$  (1.01 keV at  $z=0.99\pm0.01$ ). Allowing the widths to vary jointly, the best fit width value is  $10\pm9$  ev. To gauge the significance of these features, we simulate  $10^4$  data sets from the power-law model above. First fitting the pure power-law model, then allowing the normalizations of the Gaussian components to vary along with the power-law component, we find 0 iterations which yield a larger improvement in  $\chi^2$  than the measured value ( $\Delta\chi^2=20.2$  for 2 additional degrees of freedom). The probability that these lines are due to random Poisson fluctuations is thus <0.01%.

It will be useful below to have a computationally less intense gauge of significance, which also takes into account the number of trials performed to find a given spectral feature. Figure 2 displays the power-law model found above over-plotted on the summed HEG+MEG counts, at 3 binnings. The 1.31 keV (9.4 Å) feature is seen in both the top and middle plots at  $4.0\sigma$ . This significance describes the Poisson probability that the signal plus background counts could reach a value greater than or equal to the observed values, with the Poisson mean fixed to the number of counts predicted by the model plus the background. The probability for a chance fluctuation of this or greater significance in one or more of the  $\sim 70$  bins shown in the middle panel of Figure 2 is approximately 0.5%, calculated from  $P_N = 1 - (1 - P1)^N$ . A broad feature corresponding to the 1.01 keV line mentioned above is observed in the 1st and 3rd panels of Figure 2 at  $\sim 12.2$  Å, with a significance of  $2.9\sigma$ . There is approximately a 12% chance that one or more of the  $\sim 35$  bins in the 3rd panel should have fluctuated at or beyond the  $2.9\sigma$  level. No additional features at or above  $2.9\sigma$  appear to be present in the HETGS spectrum.

We also attempt to fit these data using a CIE plasma model, as has been done previously in the case of several recent GRB afterglows observed with XMM-Newton (R02, Watson et al. (2002)). We form the model using the APED database accessible through ISIS, with the redshift fixed at z=0.99. We utilize a turbulence velocity  $v_{\rm T}$ , fixed at 2000 km/s, and thermal line profiles to produce the best-fit line widths above. We fix the abundance of metals lighter than Mg to solar. We tie the Si abundance to the S abundance, and allow Ni to vary freely. All other metals are frozen to zero abundance. The CIE plasma fit (Figure 3,  $\chi^2_{\nu} = 177.8/152$ ) is slightly poorer than the pure power-law fit. Allowing the APED metal abundances previously set to zero to vary does not improve the fit. The best fit plasma temperature is  $9.2 \pm 1.2$  keV. The best fit S,Si abundance is  $2.9 \times \text{solar}$ , and the linked

abundance is greater than solar at 98% confidence ( $\Delta\chi^2 = 5.5$  for 1 additional parameter). The best fit Ni abundance is  $1.8 \times \text{solar}$ . There is a low ( $1.6\sigma$ ) significance detection of a Ni-K line in the MEG spectrum. This features appears as two bins modestly over the power-law fit in Figures 1, 4 near 4 keV. The APED model fits these bins with a blend of K lines from H and He-like Ni. The APED model with an abundance of Fe comparable to the Si and S abundances would produce a very strong and easily detectable Fe-K feature (Figure 4). In Table 1, we report 1-parameter 90% confidence upper limits to the abundances of several elements, with upper limits to the line fluxes and rest-frame equivalent widths of H-like K lines in each species. In Figures 5, 6, and 7 we compare the abundances, line luminosities, and rest-frame equivalent widths, respectively, to those reported for other GRB X-ray afterglows.

Since, the abundances of  $\alpha$ -particle nuclei produced by core-collapse SNe are expected to be approximately the same (see e.g. Rauscher et al. (2002)), relative to solar, the low relative upper limits we find for the abundances of Ar and Ca possibly indicate that the Si and S lines are not the result of thermal emission from a hot plasma. After radioactive decay, we would expect an Fe abundance similar to the low-Z, multiple- $\alpha$  metal abundances. This implies that the line fluxes from one or more of the Fe group elements (Fe, Ni, Co) should be higher than we observe. We discuss below the possibility that the lines are due to reflection. An alternative possibility, suggested in part by the APED model's apparent tendency to underfit the continuum below  $\sim 1.5$  keV (Figure 1), is that we must also include a power-law component. It is then possible to use the APED model with a lower temperature ( $\sim 2$  keV), and this weakens the high energy continuum and the lines from Ar, Ca, and the Fe group elements relative to the Si and S lines. We find models with a single abundance for the  $\alpha$ -particle nucleii and Fe which improve upon the power-law fit but do not appear to be as good as the power-law plus two Gaussian fit. Finally, we note that the abundances quoted in Table 1 lose meaning if a power-law component is also present.

#### 3.2. GRB 021004

An absorbed power-law fit to the 1st-order spectra does not require an absorption column in excess of the Galactic value, as reported by Sako & Harrison (2002). Therefore, in each model that we consider, we include absorption with  $N_{\rm H}$  frozen to  $4.24 \times 10^{20}$  cm<sup>-2</sup>.

The data are very well fit by a power-law (Figure 8,  $\chi^2_{\nu} = 39.5/55$ ), with  $\Gamma = 2.01 \pm 0.08$  and normalization  $(1.7 \pm 0.1) \times 10^{-4}$  photons/keV/cm<sup>2</sup>/s at 1 keV, consistent with the values found by Sako & Harrison (2002) and Holland et al. (2002). A thermal bremsstrahlung fit is a somewhat poorer, though still very acceptable, fit ( $\chi^2_{\nu} = 47.2/55$ ), with kT = 3.2 ± 0.4 keV. We find consistent fits using the 0th-order data.

We plot the combined HEG/MEG data in count space with the power-law model overplotted in Figure 9, for the same binnings as in Figure 2. No significant features are observed. The largest fluctuation occurs in the middle panel, where one of the  $\sim 70$  bins reaches  $2.6\sigma$ . There is approximately a 44% chance that this would happen by chance in one or more of the bins in that plot.

## 4. Temporal Analysis

As displayed in Figure 10, the afterglow continua, though moderately variable in the case of GRB 021004, do not appear to evolve spectrally. To search for time-variable discrete features, we divide the summed HEG+MEG data sets into 2, 4, or 8 portions of equal numbers of counts. For each time section, we examine the counts data at 3 binnings: 0.11, 0.21, and 0.42 Å (as in Figures 2, 9). For each GRB afterglow, we fit absorbed power-law's to each of these 42 data sets by minimizing the Cash statistic (Cash 1979). We then search the bins between 1 and 16 Å where the expected number of counts is greater than 1 for deviations from the best fit model, interpreting the deviations using Poisson statistics as in Section 3. To estimate the trials probabilities  $P_N$ , we take for N the number of bins into which the entire data set has been divided. For example, dividing the GRB 020813 data into 8 time sections at 0.11 Å binning, we find 899 bins expected to contain more than 1 counts. We report only the detections for which  $P_N < 0.5$ . For each detection of an emission (absorption) feature, we check that positive (negative) deviations from the model are present in both the MEG and HEG. Our results, summarized below, are shown in Table 2.

#### 4.1. GRB 020813

Searching through time slices in the data as described above, we find 17 features over threshold. Possible identifications are shown in Table 2, along with significances and equivalent width estimates. The strongest detections (peaking at  $4.4\sigma$ ) are of the S XVI K $\alpha$  line. This line appears to be brighter early in the observation (especially during the first 12 ksec), though it is also detected in the final 28 ksec. In Figure 11, we plot the S XVI K $\alpha$  line flux (measured with Gaussian fits of fixed width and location) and the continuum flux versus time. Using the likelihood ratio test, we find evidence for a decrease in equivalent width between the first 28.5 ksec of data and the remainder of the observation at 97% confidence ( $\Delta \chi^2 = 4.7$  for 1 additional parameter). We detect the Si XIV K $\alpha$  line throughout the observation, with the line peaking (3.6 $\sigma$ ) somewhat later than the S line.

There are also detections of moderate significance just beyond 6 and 8 Å, which may be due to Ca and Ar, respectively. The Ca features appear in emission, then in absorption. The Ar features appear in absorption, then in emission. Also, if the implied redshift of an Ar K-line is to agree within errors with the value estimated above for the S and Si lines, the Ar would need to be in an ionization state lower than the He-like species. Although the Ca and Ar features are near the instrumental Ir-M and Al-K edges, respectively, the calibration of these edges is good enough that we do not associate the features with the detector.

Finally, there are 3 weak  $(P_N \sim 0.5)$  detections, which can be associated with transitions in Al and Na, as shown in Table 2.

## 4.2. GRB 021004

We find 2 bins over threshold (Table 2) in time sections of the GRB 021004 afterglow spectrum. The weaker of these (with  $P_N \approx 0.5$ ) is not consistent between the HEG and MEG and is clearly due to the detector Si-K edge. A possible identification for the other (absorption) feature is Ca XX K $\alpha$ , blue-shifted from the host galaxy at z = 2.328 (Mirabel et al. 2002) by 0.13c.

A conservative estimate for the expected number of chance emission or absorption line detections, given our thresholding scheme is  $2*log(2)*3*3 \approx 12$ . This takes into account that we have searched for emission and absorption features in 9 (3 binnings × 3 time sectionings) data sets, where the expected number of chance detections is approximately log(2) for each data set. This estimate is an upper limit as the 9 data sets are correlated. For GRB 020813 the number of detections was well in excess of 12, while there were only 2 detections for GRB 021004. Most likely, we have detected only a chance deviation from the model in the case of this afterglow.

## 5. Discussion

The most significant discrete feature we observe in afterglow spectrum of GRB 020813 is clearly the line we associate with S, which we observe near  $4.0\sigma$  in the full data set and near  $4.4\sigma$  during the first 12 ksec. For the full observation no detector anomalies (e.g. flares, flickering pixels) are observed in the ACIS-S CCD regions yielding the HETGS MEG/HEG  $\pm 1$  order counts from this line. The background is negligible between 0.6 and 6 keV, contributing only 3% of the total counts. Pileup in the grating spectrum is not a concern for this observation due to the very low count rate. Excess counts corresponding

to the S line are detected in each independent spectrum (MEG/HEG  $\pm 1$  orders), and the numbers are consistent at the  $1.5\sigma$  level. The combined 1st-order spectra (MEG/HEG) show a consistent number of excess counts at the  $1\sigma$  level. The validity of this line detection and its association with S XVI K $\alpha$  are strengthened by the detection of a line at the expected energy for Si XIV K $\alpha$ , and possibly also by low-significance detections of the K lines from Ar, Ca, and Ni. We have performed a parallel reduction for the GRB 021004 afterglow data, and this has yielded no convincing evidence for discrete spectral features.

Although we find marginal evidence for temporal variability in the line emission for GRB 020813 (Section 4), the lines are detected in the full 76.8 ksec observation, and the full data set is moderately well fit by a plasma in collisional ionization equilibrium (Section 3). The lines are blue-shifted by  $\sim 0.1c$  and this strongly suggests that the emitting material resides within an expanding SN shell. For radially expanding emitting material, the narrowness of the lines requires that the emission comes from only a small solid angle ( $\Omega \leq 0.4$ ), as viewed from the GRB, consistent with GRB beaming models (Frail et al. 2001). The line duration ( $t_{\rm line} \gtrsim 76.8$  ksec) can be attributed to time delays across a thin shell, and this requires a radius R for the emitting material  $R = \frac{ct_{\text{line}}}{1+z} \frac{2\pi}{\Omega} \gtrsim 10^{16} \text{ cm}$ . An estimate  $R \lesssim 10^{18} \text{ cm}$  for the maximum likely R is determined using the smallest solid angle found for a GRB jet in Frail et al. (2001). Assuming an optical depth to Thomson scattering  $\tau_{\rm T} \sim 1$ , this range of possible shell radii translates into a mass range for the emitting material:  $1M_{\odot} \gtrsim M \gtrsim 10^4 M_{\odot}$ . The required mass, which increases as  $R^2$ , is reduced if the emitting material is clumped, rather than uniformly spread across the shell. In the case of GRB 011211, R02 assert that a shell of thermal plasma at  $R \sim 10^{15}$  cm can account for the afterglow spectrum and for the duration of the reported emission lines. Taking into account radiation transfer across the shell, Lazzati (2002) argues that a larger radius is required ( $R \gtrsim 10^{17}$  cm), because the large afterglow luminosity implies a high density, which implies a cooling time much shorter than the observed line duration. Following Lazzati (2002), we find that a thermal model for GRB 020813 also implies  $R \gtrsim 10^{17}$  cm, except for the case (discussed below) where the luminosity of the thermal component is actually overwhelmed by a ( $\sim 10 \times$  brighter) power-law continuum component. In this case, a solution with  $R \sim 10^{16}$  cm is possible. The density is low  $(n \sim 10^8 \text{ cm}^{-3})$ , and this implies a shell with thickness  $dR \sim R$  for  $\tau_T = 1$ . At larger radii, the shell must be either very thin or very clumped for the contained mass to be similar to that expected from SNe ( $M_{\rm ejecta} \lesssim 20 M_{\odot}$ , Woosely & Weaver (1995)).

We see three reasons, which arise from complexities in our modeling, to be cautious in interpreting our results as evidence for a persistent thermal component. First, we observe lines with best fit widths an order of magnitude larger than the thermal line widths. We account for this in the thermal model by introducing a turbulence velocity of 2000 km/s. It is also possible that this broadening is kinematical. Second, the best-fit CIE plasma model

has marginally dissimilar abundances for the multiple- $\alpha$  elements (Figure 5) and very low abundances for the Fe group elements relative to the multiple- $\alpha$  elements (Figure 5, Figure 4). This would require an unusual chemical composition for the emitting medium, a mechanism beyond the APED model for suppressing emission from metals other than Si and S, or the addition of a power-law continuum component to the model as discussed in Section 3. Third, the data do not tightly constrain the relative contributions to the continuum from the CIE plasma and from this possible power-law component. Indeed, the continuum appears nonthermal, as would be expected for the X-ray afterglow of the burst. The predominance of a power-law component may also be suggested by our measured S XVI K $\alpha$  and Si XIV K $\alpha$ rest-frame equivalent widths. These are an order of magnitude smaller than those found in R02, while the line fluxes are similar (Figures 7 and 6). Figure 11 shows the continuum and line fluxes for both afterglows, with redshift effects taken out. A simple interpretation of the data in that figure is that the line emission is powered by the GRB flux, which is similar  $(E_{\rm ISO} \sim 10^{52} {\rm ergs})$  for GRB 011211 and GRB 020813, rather than by the afterglow flux, which is very different. The line emission may occur later and last longer for GRB 020813 than for GRB 011211 because the emitting material lies at a larger R.

Though these considerations do not rule out a thermal model, reflection models may more naturally describe a spectrum with broad lines superposed on a power-law continuum (see e.g. Ballantyne et al. (2001), Vietri et al. (2001)). In these models, the line broadening is due to Compton scattering. If the electron temperature is similar to the line energy, we expect  $\sigma_E/E \sim (kT/m_ec^2)^{1/2} \sim 0.05$  (at 1.3 keV) for a single scattering. Because this is already a factor  $\sim 5 \times$  larger than the observed widths, we require the reflector to not be highly ionized. Consulting Figure 2 of Lazzati, Ramirez-Ruiz, & Rees (2002), it appears that our observed dissimilarity in line luminosities (Table 1, Figure 6) may further reinforce this conclusion. Their reflection models with ionization parameter  $\xi$  in the range  $10 < \xi < 100$  can produce Si and S line luminosities which are an order of magnitude greater than luminosities of lines from Ar, Ca, and Fe. Fit-able versions of these models will be necessary to check whether the GRB 020813 data are more likely produced under reflection than by a thermal mechanism. A geometry will also need to be found which can reproduce the observed blue-shift and line timescales (see Vietri et al. (2001) for examples).

In conclusion, we detect blue-shifted lines from an over-abundance of light metals characteristically produced in massive stars during pre-supernova nucleosynthesis in the X-ray afterglow of GRB 020813. Two lines of evidence point toward a two-step explosion, as in the supranova model (Vietri & Stella 1999). The outer layers of the star ejected in the SN would be expected to contain a large over-abundance of Ni<sup>56</sup> relative to the other Fe group elements (i.e. Fe and Co). Ni<sup>56</sup> decays to Co<sup>56</sup> with a half-life of 6 days, and Co<sup>56</sup> decays to Fe<sup>56</sup> with a half-life of 78 days. Our weak detection of a Ni feature, with no detection of Fe (or Co),

suggests a very short time delay ( $\lesssim 1$  week) between the SN and the GRB. The narrowness and longevity of the emission lines suggests a longer time delay ( $\gtrsim 2$  months). A thermal model adequately fits the full data set. A bright Fe (or Ni or Co) feature is not observed, however, and this is perhaps the strongest reason to favor a reflection model, where an Fe line can be quenched by Auger auto-ionization (Lazzati et al. 2002).

We thank Harvey Tananbaum for his generous allocation of Director's Discretion Time for these observations. This research was supported in part by NASA contract NASW-4690.

## REFERENCES

Antonelli, L. A., et al. 2000, ApJ, 545, L39

Ballantyne, D. R., et al. 2001, ApJ, 559, L83

Bloom, J. S., et al. 1999, Nature, 401, 453

Borozdin, K. N., & Trudoyubov, S. P. 2002, astro-ph/0205208

Cash, W. 1979, ApJ, 228, 939

Fox, D. W., & Blake, C. 2002, GCN #1470

Fox, D. W. 2002, GCN #1564

Frail, D. A., et al. 2001, ApJ, 562, L55

Galama, T., et al. 1998, Nature, 395, 670

Halpern, J., et al. 2002, GCN #1578

Holland, S. T., et al. 2002, astro-ph/0211094

Jansen, F. et al. 2001, A&A, 365, L1

Kouveliotou, C., et al. 1993, ApJ, 413, L101

Kulkarni, S. R., et al. 1998, Nature, 395, 663

Kulkarni, S. R., et al. 1999, Nature, 398, 389

Lazzati, D. 2002, astro-ph/0210301

Lazzati, D., Ramirez-Ruiz E., & Rees, M. J. 2002, ApJ, 572, L57

Malesani, D., et al. 2002, GCN #1500

Marshall, H. L., et al. 2002, ApJ, 564, 941

McLaughlin, G. C., et al. 2002, ApJ567, 454

Mirabel, N., et al. 2002, GCN #1618

Piro, L., et al. 1999, A&AS, 138, 431

Piro, L., et al. 2000, Science, 290, 955

Price, P. A., et al. 2002, GCN #1475

Rauscher, T., et al. 2002, ApJ, 576, 323

Reeves, J. N., et al. 2002, Nature, 415, 512 (R02)

Reeves, J. N., et al. 2002, astro-ph/0206480

Reichart, D. E. 2001, ApJ, 554, 643

Ricker, G. R. et al. 2003, WH2001<sup>8</sup>

Rutledge, S., & Sako, M. 2002, MNRAS Submitted, (astro-ph/0206073)

Sahu, K. C., et al. 1997, Nature, 387, 476

Sako, M., & Harrison, F. A. 2002, GCN #1624

Shirasaki, Y., et al. 2002, GCN #1565

Vanderspek, R., et al. 2002, GCN #1504

Vietri, M., & Stella, L. 1999, ApJ, 527, L43

Vietri, M., et al. 2001, ApJ, 550, L43

Villasenor, J., et al. 2002, GCN #1471

Watson, D., et al. 2002, A&A, 393, L1

<sup>&</sup>lt;sup>8</sup>WH2001 = Gamma-Ray Burst and Afterglow Astronomy 2001: A Workshop Celebrating the First Year of the HETE Mission, Woods Hole, MA, November 2001, to be published in the AIP Conference Proceedings (AIP Press: New York)

Weisskopf, M. C., et al. 2002, PASP, 114, 1

Woosely, S. E., & Weaver, T. A. 1995, ApJS, 101, 181

Yoshida, A., et al. 1999, A&AS, 138433

This preprint was prepared with the AAS LATEX macros v5.0.

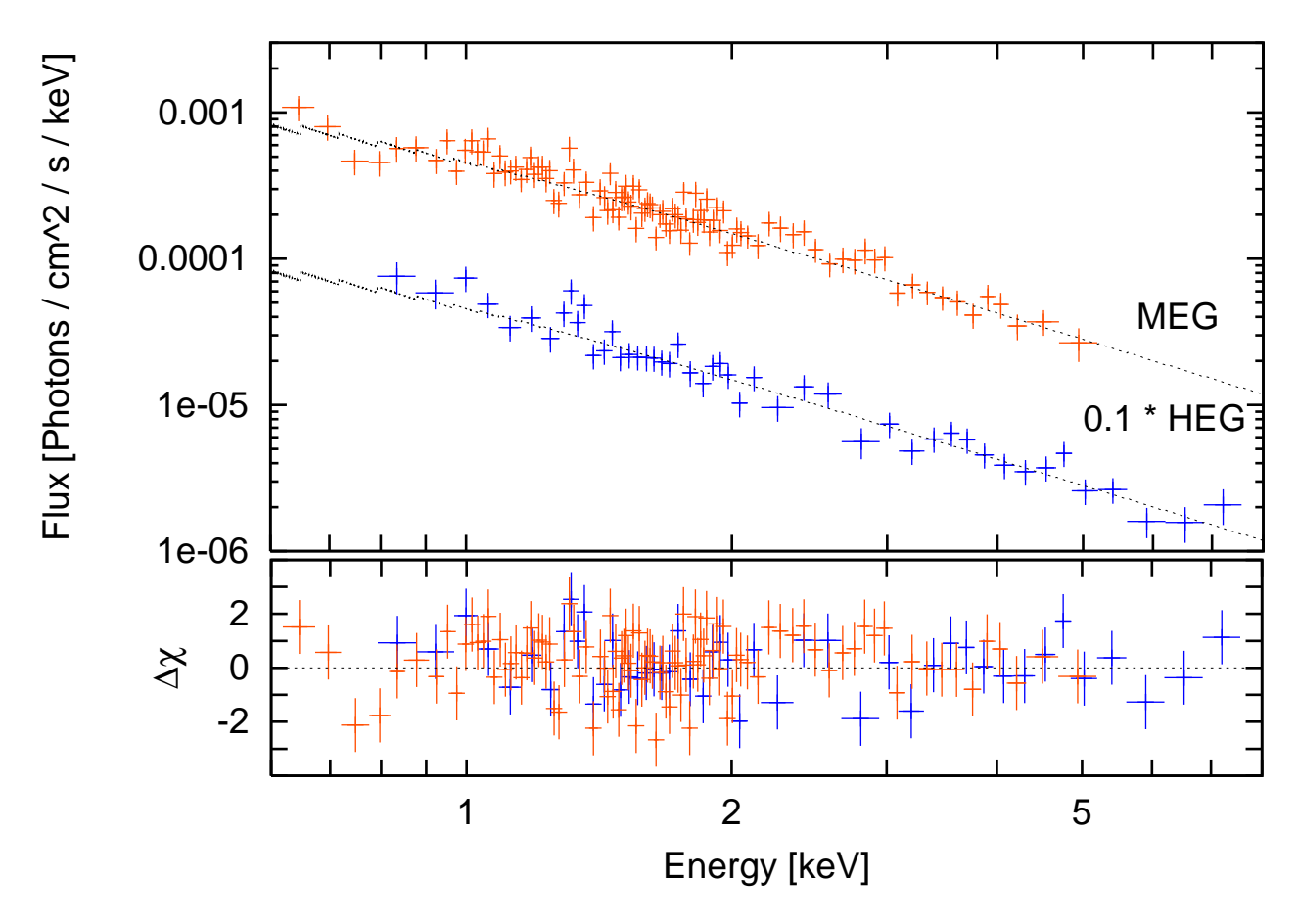


Fig. 1.— The flux-corrected HETGS spectrum for GRB 020813, with the best-fit power-law plus Galactic absorption over-plotted. Since the response matrix is diagonal at these binnings, we fit the model to the flux-corrected data directly instead of folding the model through the response prior to fitting to the counts data. The HEG data and model have been multiplied by 0.1 for ease of viewing.

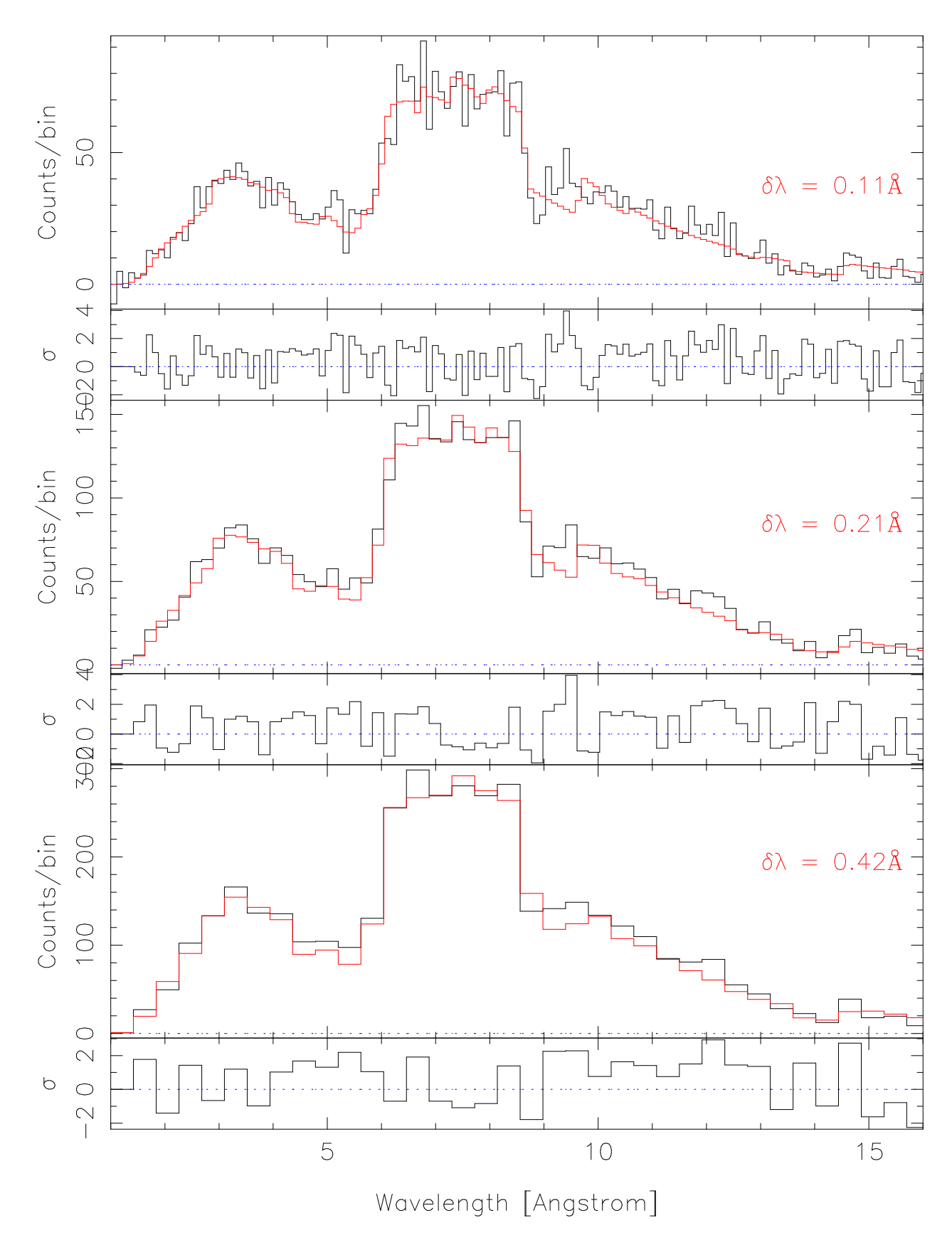


Fig. 2.— The best fit power-law model (red curve) on top of the combined HETGS HEG+MEG data, at 3 binnings, for GRB 020813. The significance (reported in  $\sigma$  units) of deviations from the model are calculated using Poisson statistics. We associate the residuals

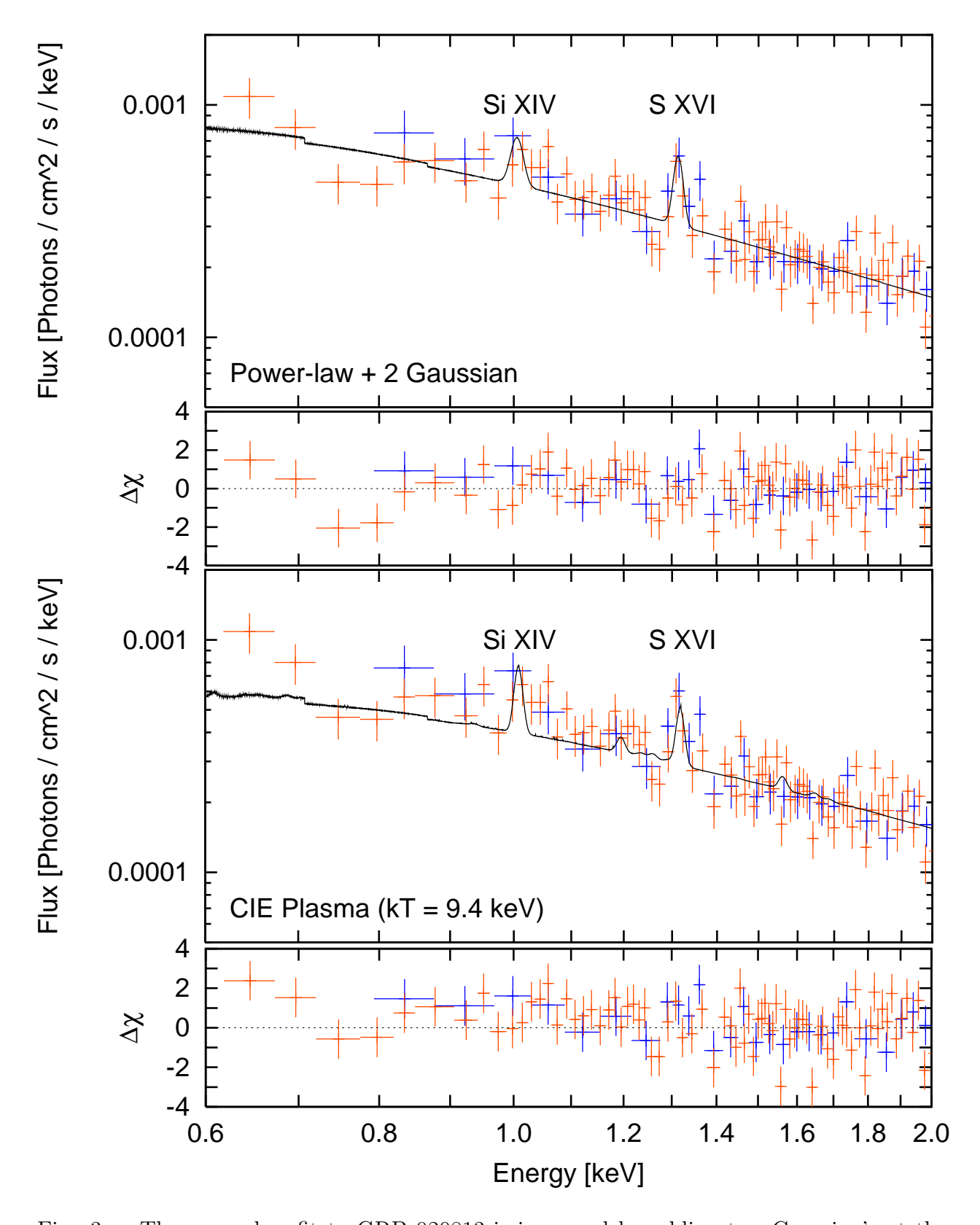


Fig. 3.— The power-law fit to GRB 020813 is improved by adding two Gaussian's at the engergies of blue-shifted (by 0.12c) S XVI K $\alpha$  and Si XIV K $\alpha$ . The lines and continuum can be modelled less effectively by a CIE plasma model (bottom plot) containing S, Si, and Ni. HEG data are in red; MEG data are in blue.

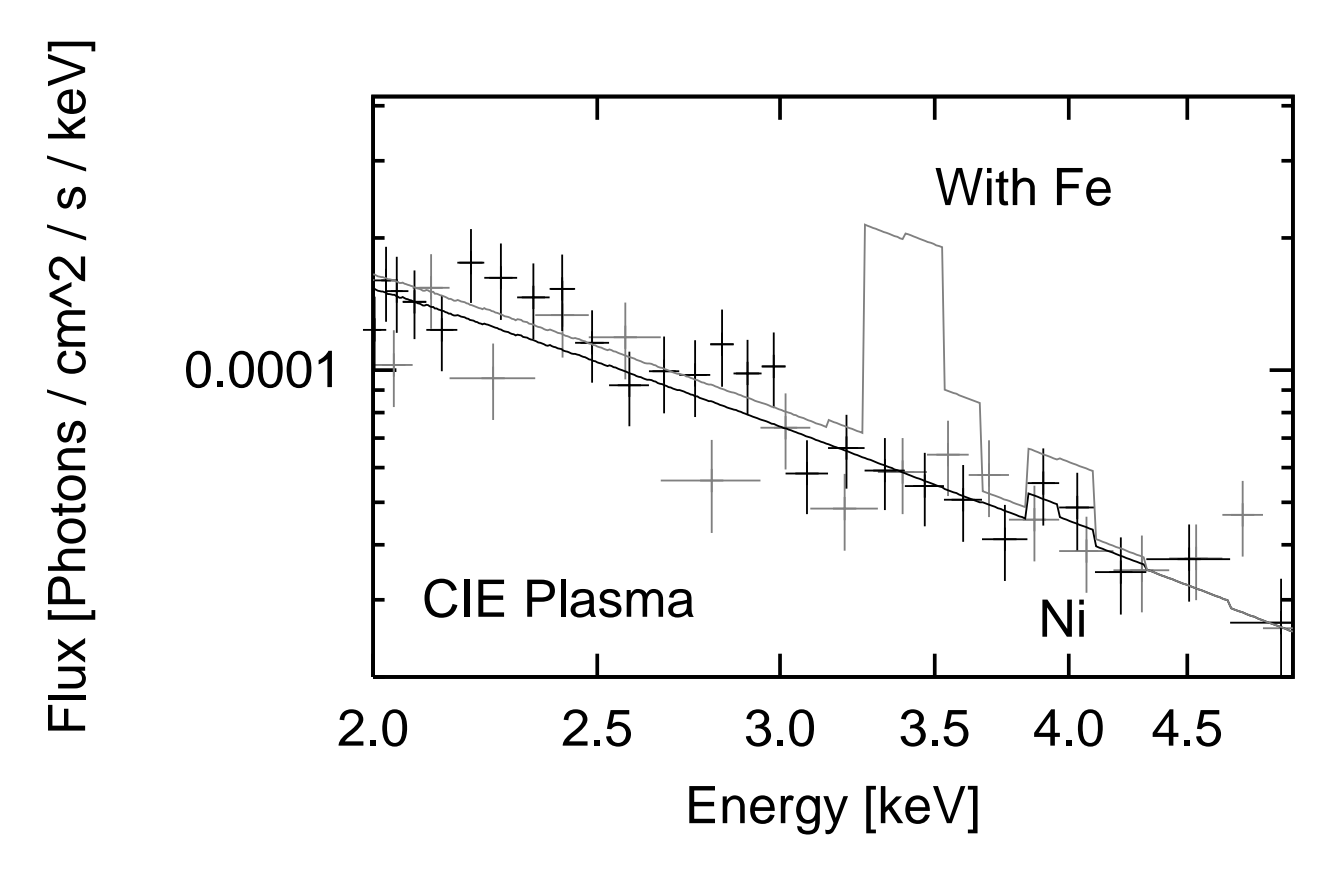


Fig. 4.— Though the best-fit CIE plasma model contains a  $1.8 \times \text{solar}$  abundance of Ni, an equivalent abundance (similar to the inferred Si and S abundances) of Fe is strongly ruled out. HEG data are in grey; MEG data are in black.

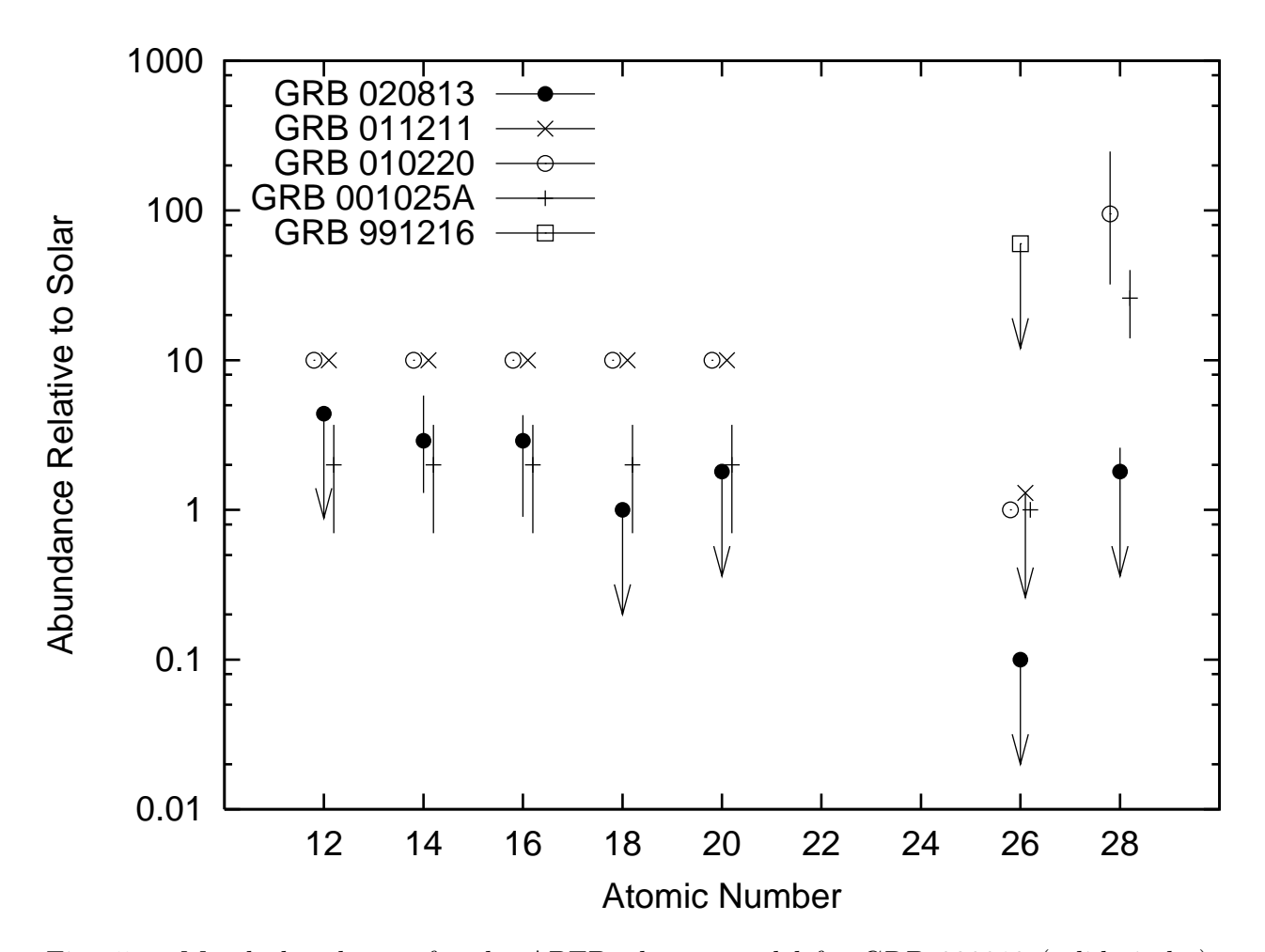


Fig. 5.— Metal abundances for the APED plasma model for GRB 020813 (solid circles), as in Table 1. Also plotted are the abundances reported in the literature for several other GRB X-ray afterglow spectra. The values for GRB 011211 come from R02. The values for GRB 010220 and GRB 001025A come from Watson et al. (2002). The value for GRB 991216 has been taken from Piro et al. (2000). Error bars have been plotted where available.

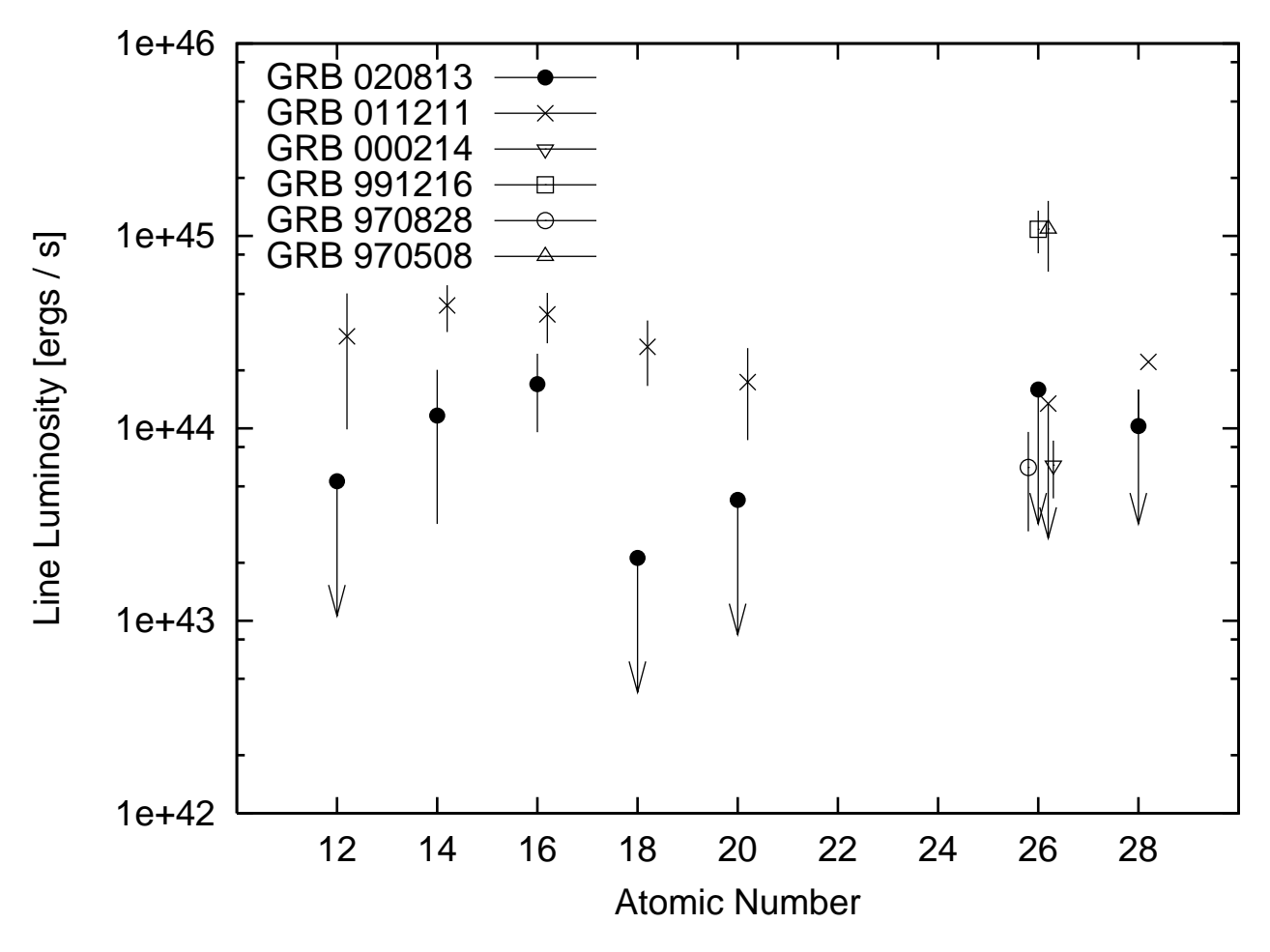


Fig. 6.— Isotropic equivalent line luminosities from Gaussian fits (Table 1) for GRB 020813 (solid circles, host at z=1.254) and for several other GRBs in the literature. To determine luminosity distances, we use a cosmology with  $\Omega_m=0.3$ ,  $\Omega_{\Lambda}=0.7$ , and h=0.65. The values for GRB 011211 come from R02, with z=2.14. The value for GRB 000214 comes from Antonelli et al. (2002), with z=0.47. The value for GRB 991216 has been taken from Piro et al. (2000), using z=1. The value for GRB 970828 comes from Yoshida et al. (1999), using z=0.33. The value for GRB 970508 comes from Piro et al. (1999), using z=0.835. Error bars have been plotted where available.

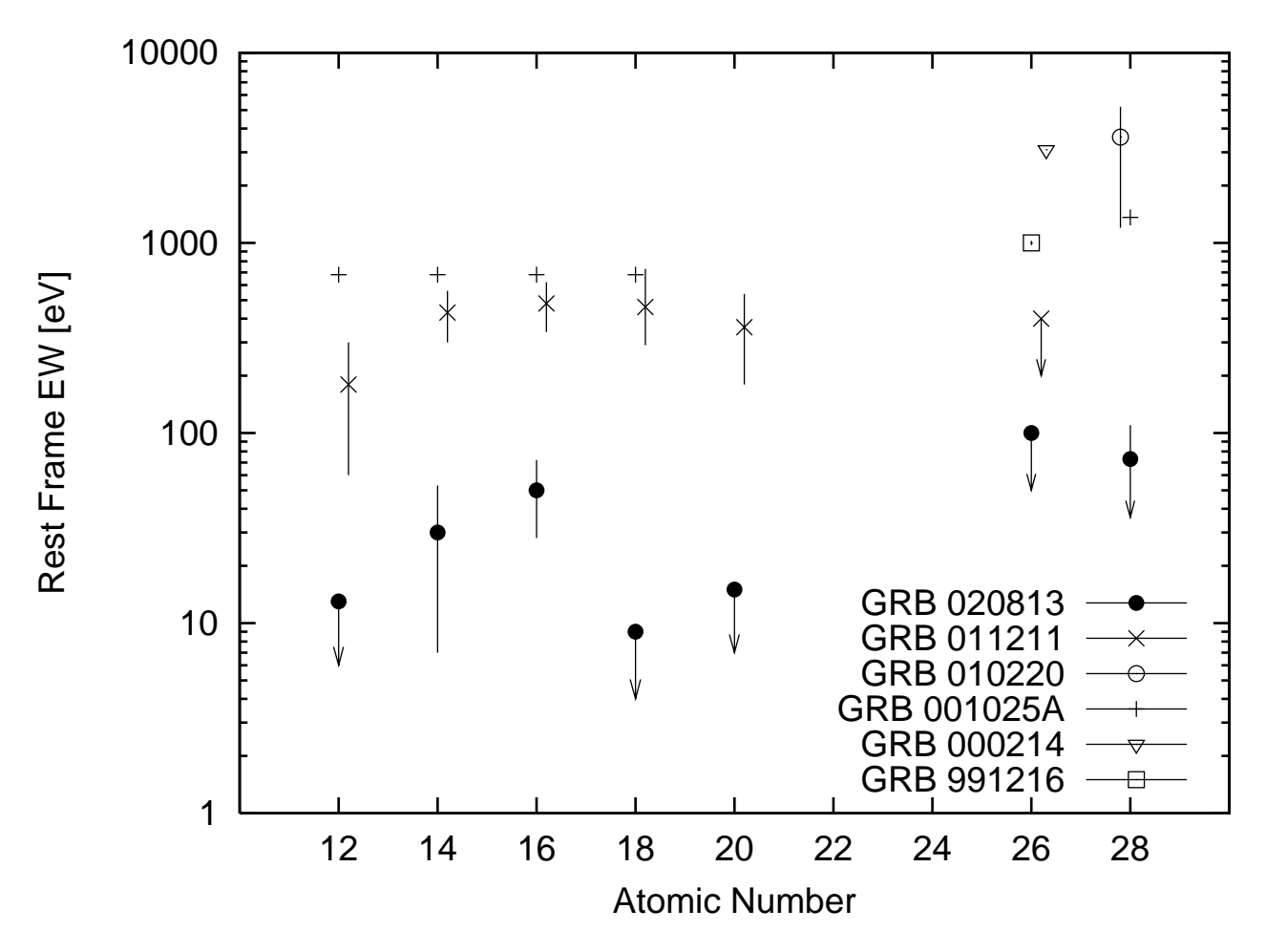


Fig. 7.— Rest-frame equivalent widths in eV from Gaussian fits (Table 1) for GRB 020813 (solid circles, z=0.99) and for several other GRBs in the literature. The values for GRB 011211 come from R02, with z=1.88. The values for GRB 010220 (z=1.0) and GRB 001025A (z=0.7) come from Watson et al. (2002). The value for GRB 000214 comes from Antonelli et al. (2002), with z=0.47. The value for GRB 991216 has been taken from Piro et al. (2000), using z=1. Error bars have been plotted where available.

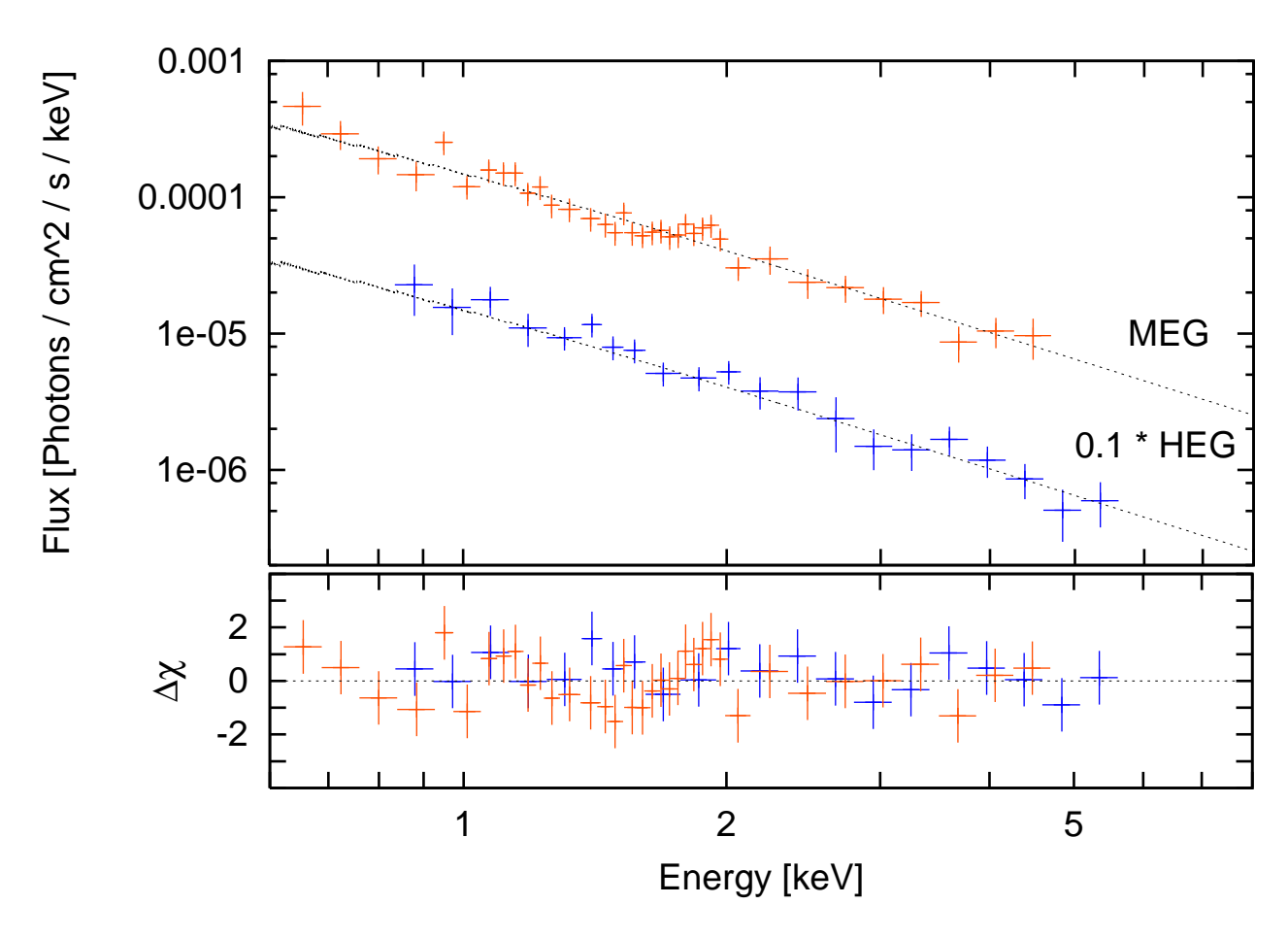


Fig. 8.— The flux-corrected HETGS spectrum for GRB 021004, with the best-fit power-law plus Galactic absorption over-plotted. The HEG data and model have been multiplied by 0.1 for ease of viewing.

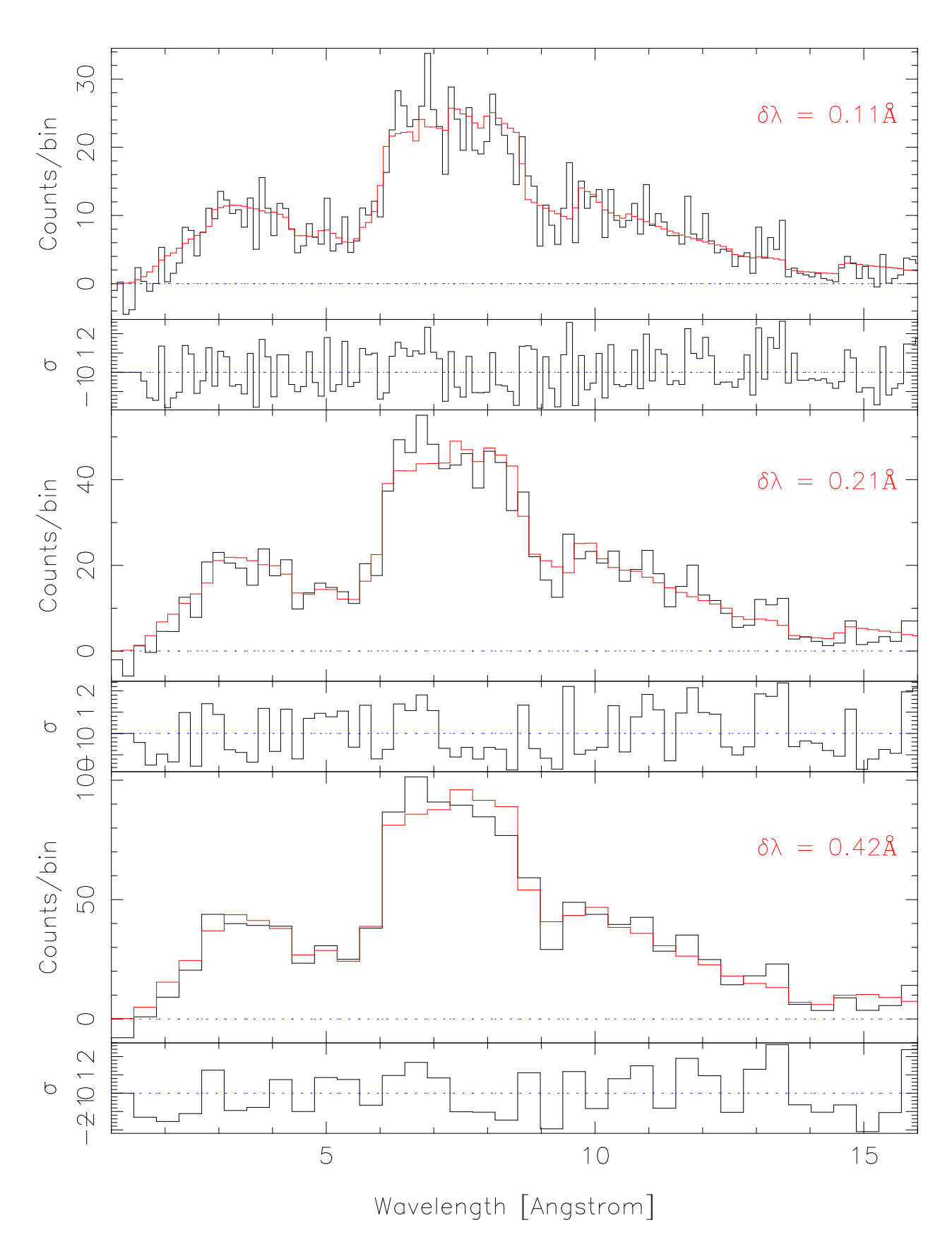


Fig. 9.— The best fit power-law model (red curve) on top of the combined HETGS HEG+MEG data, at 3 binnings, for GRB 021004. No highly significant deviations from the model are observed.

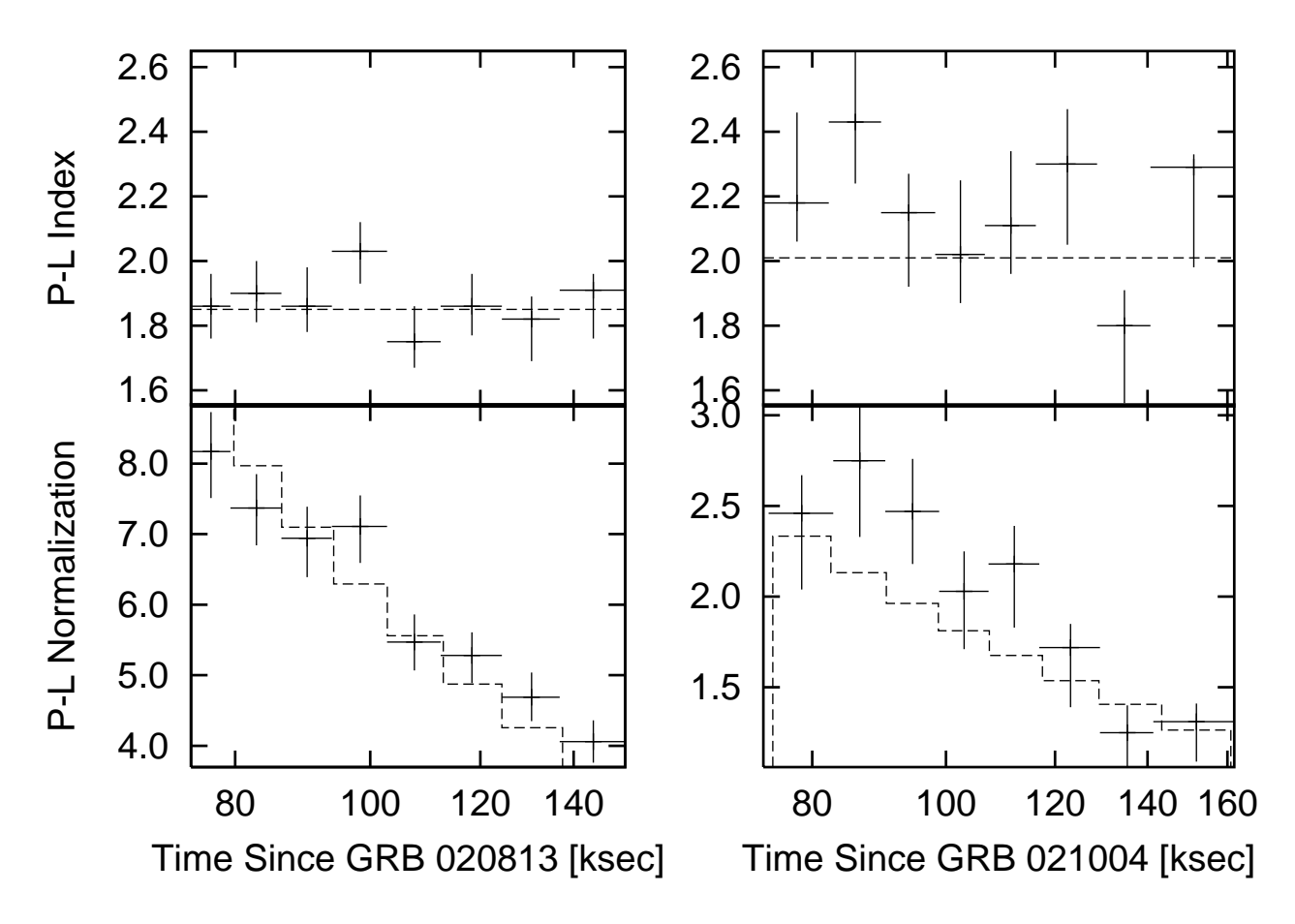


Fig. 10.— To look for spectral variability, the HETGS data for each GRB are divided into 8 regions of equal counts and fit with absorbed power-laws by minimizing the Cash statistic (Cash 1979). The above plots show the power-law indeces  $\Gamma$  and the power-law normalizations found for each fit, with the fits derived for the entire data set overplotted as dashed lines. Error bars are 90% confidence, determined from the 1-parameter confidence intervals.

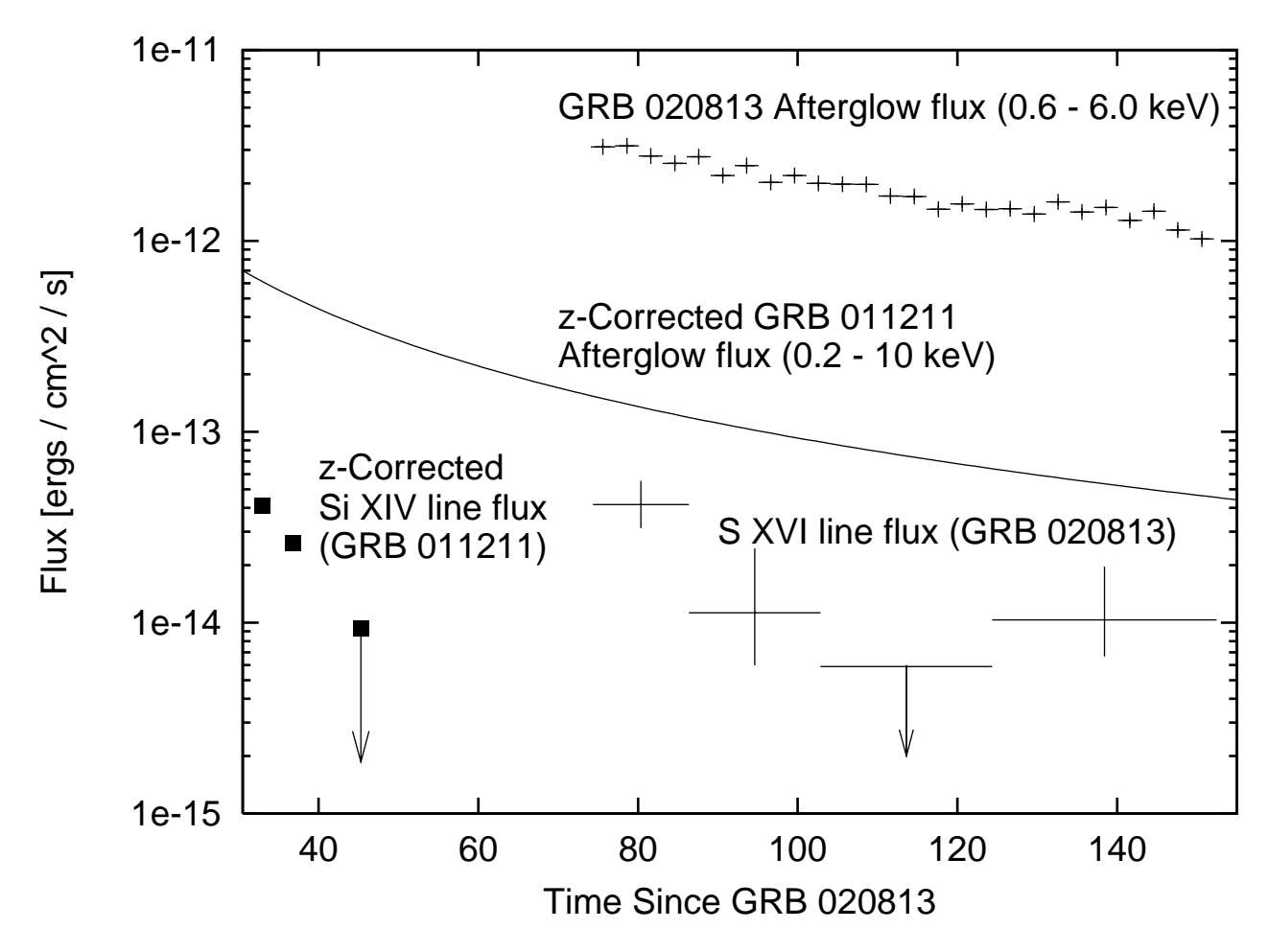


Fig. 11.— The points on the left show the Si XIV K $\alpha$  line flux for GRB 011211 from R02, corrected to the redshift of GRB 020813. The integrated afterglow flux for GRB 012111 is also plotted and extrapolated. We employ a cosmology with  $\Omega_m = 0.3$ ,  $\Omega_{\Lambda} = 0.7$ , and h = 0.65. At a later time ( $\sim 50$  ksec later in the GRB frame), we measure a similar line flux. However, the GRB 020813 afterglow flux is approximately an order of magnitude higher that that of GRB 011211. On the right, we plot the measured line flux from S XVI K $\alpha$ , and the afterglow flux, versus time since GRB 020813. Error bars and the one upper limit are at  $1\sigma$  confidence.

Element	Abund.	Flux	EW [eV]
Mg	4.4	0.5	13
Si	5.8	1.9	53
	$(2.9^{+2.9}_{-1.6})$	$(1.1 \pm 0.8)$	$(30 \pm 23)$
S	4.3	2.3	72
	$(2.9^{+1.4}_{-2.0})$	$(1.6 \pm 0.7)$	$(50 \pm 22)$
Ar	1.0	0.2	9
Ca	1.8	0.4	15
Fe	0.1	1.5	100
Ni	4.4	1.5	110
_	$(1.8^{+2.6}_{-1.8})$	$1.0^{+0.5}_{-1.0}$	$73^{+37}_{-73}$

Table 1: 90% confidence upper limits for APED model elemental abundances, K-shell line fluxes ( $\times 10^{-14}$  ergs cm<sup>-2</sup> s<sup>-1</sup>), and rest-frame K-shell line equivalent widths, determined from power-law plus Gaussian fits. The observer-frame line widths were set via  $dE/E = v_t/c \approx 0.0067$ . Line centers are set with z = 0.99, as observed for the S and Si lines.

GRB 020813						
$\lambda$	$d\lambda$	$\sigma$	$P_N$	EW (eV)	Time	ID
6.25	0.42	3.0	0.4765	$137 \pm 54$	2nd-8th	Ca XX+XIX $(z = 1.01 \pm 0.07)$
6.14	0.21	-3.3	0.4741	$-96 \pm 19$	3rd-8th	Ca XX $(z = 1.03 \pm 0.07)$
6.14	0.21	-3.1	0.4115	$-66 \pm 17$	2nd- $Q$ tr	Ca XX $(z = 1.03 \pm 0.07)$
8.25	0.21	-3.1	0.3772	$-36 \pm 9$	1st- $Qtr$	Ar XVII $(z = 1.09 \pm 0.03)$
8.21	0.11	3.5	0.3160	$53 \pm 20$	3rd-8th	Ar XVII $(z = 1.08 \pm 0.01)$
8.35	0.42	3.3	0.1473	$57 \pm 20$	2nd- $Q$ tr	Ar XVII $(z = 1.11 \pm 0.05)$
9.50	0.21	4.4	0.0034	$78 \pm 24$	1st- $Qtr$	S XVI $(z = 1.00 \pm 0.02)$
9.50	0.21	3.2	0.4973	$77 \pm 32$	2nd-8th	S XVI $(z = 1.00 \pm 0.02)$
9.53	0.11	3.5	0.1051	$31\pm11$	1st-Half	S XVI $(z = 1.01 \pm 0.01)$
9.50	0.21	3.9	0.0150	$45\pm14$	1st-Half	S XVI $(z = 1.00 \pm 0.02)$
9.41	0.11	3.9	0.0529	$55 \pm 19$	4th- $Q$ tr	S XVI $(z = 0.98 \pm 0.01)$
12.50	0.11	3.6	0.1821	$39 \pm 16$	2nd- $Q$ tr	Si XIV $(z = 1.02 \pm 0.01)$
12.13	0.42	2.7	0.3674	$36 \pm 16$	2nd-Half	Si XIV $(z = 0.96 \pm 0.03)$
14.65	0.42	3.0	0.3188	$70 \pm 30$	3rd- $Qtr$	Al XIII $(z = 1.04 \pm 0.03)$
14.65	0.42	2.7	0.4261	$41\pm19$	2nd-Half	Al XIII $(z = 1.04 \pm 0.03)$
15.07	0.42	-2.6	0.4718	$-28 \pm 8$	1st-Half	Na XI K-edge ( $z=1.00\pm0.03$ )
GRB 021004						
$\lambda$	$d\lambda$	$\sigma$	$P_N$	EW (eV)	Time	ID
8.54	0.11	-3.4	0.1850	-31±5	1st-Half	Ca XX $(z = 1.83 \pm 0.02)$
6.67	0.42	2.6	0.4962	$91 \pm 42$	1st-Half	Detector Si K-edge

Table 2: Features detected in the GRB spectra during various time slices, at binning  $d\lambda$ . Unless otherwise noted, line ID's refer to the K $\alpha$  lines of each species. The redshift associated with each ID is absolute, rather than relative to the systematic redshifts measured in the optical (z=1.254 for GRB 020813; z=2.328 for GRB 021004). The significances for individual deviations ( $\sigma$  values) are determined from the observed counts over the expected model and background values, using Poisson statistics. The significance given N trials can be estimated by  $P_N$  (Section 3). Rest-frame equivalent widths are estimated as  $(1+z)dE(cts/cts_{model}-1) \pm (1+z)dE\sqrt{cts}/cts_{model}$ , with z=0.99 for GRB 020813 and z=2.328 for GRB 021004. For each observation, time regions are contiguous: the 1st-Qtr includes the 1st and 2nd-8th's, etc.

GRB 020813: 1st-8th 0-5, 2nd-8th 5-12, 3rd-8th 12-19.5, 4th-8th 19.5-28.5, 5th-8th 28.5-38, 6th-8th 38-50, 7th-8th 50-62.5, and 8th-8th 62.5-78.1 ksec after the start of the observation.

GRB 021004: 1st-Half 5-33 ksec after the start of the observation.